ULTRAFAST STRUCTURAL CHANGES WITHIN A PHOTOSYNTHETIC REACTION CENTRE

Robert Dods[1†], Petra Båth[1†], Dmitry Morozov[2], Viktor Ahlberg Gagnér[1], David Arnlund[1], Hoi Ling Luk[2], Joachim Kübel [1], Michał Maj[1], Adams Vallejos[1], Cecilia Wickstrand[1], Robert Bosman[1], Kenneth R. Beyerlein[3], Garrett Nelson[4], Mengning Liang[6], Despina Milathianaki[6], Joseph Robinson[6], Rajiv Harimoorthy[1], Peter Berntsen[1,7], Erik Malmerberg[8], Linda Johansson[1,9], Rebecka Andersson[1], Sergio Carbajo[6], Elin Claesson[1], Chelsie E. Conrad[5], Peter Dahl[1], Greger Hammarin[1], Mark S. Hunter[6], Chufeng Li[4], Stella Lisova[4], Antoine Royant[10,11], Cecilia Safari[1], Amit Sharma[1], Garth J. Williams[6], Oleksandr Yefanov[3], Sebastian Westenhoff[l], Jan Davidsson[12], Daniel P. DePonte[6], Sébastien Boutet[6], Anton Barty[3], Gergely Katona[1], Gerrit Groenhof[2], Gisela Brändén[1], Richard Neutze[1]*

[1]*Department of Chemistry and Molecular Biology, University of Gothenburg, Gothenburg, Sweden.*

[2]*Nanoscience Center and Department of Chemistry, University of Jyväskylä, Jyväskylä, Finland.*

[3]*Centre for Free-Electron Laser Science, Deutsches Elektronen-Synchrotron DESY, Hamburg, Germany.*

[4]*Department of Physics, Arizona State University, Tempe, Arizona, USA.*

[5]*Department of Chemistry and Biochemistry, Arizona State University, PO Box 871604, Tempe, AZ 85287-1604, USA.*

[6]*Linac Coherent Light Source, Stanford Linear Accelerator Centre (SLAC) National Accelerator Laboratory, Menlo Park, CA, USA.*

[7]*Australian Research Council Centre of Excellence in Advanced Molecular Imaging, La Trobe Institute for Molecular Science, La Trobe University, Melbourne 3086, Australia*

[8]*Molecular Biophysics and Integrated Bioimaging, Lawrence Berkeley National Laboratory, Berkeley, CA, USA.*

[9]*The Bridge Institute, Department of Chemistry, University of Southern California, Los Angeles, CA 90089-3303, USA.*

[10]*Institut de Biologie Structurale (IBS), Université Grenoble Alpes, CEA, CNRS, F-38000 Grenoble, France*

[11]*European Synchrotron Radiation Facility, F-38043 Grenoble, France.*

[12]*Department of Chemistry-Ångström laboratory, Uppsala University, Uppsala, Sweden.*

[†]These authors contributed equally to this work.

**Corresponding author:* richard.neutze@gu.se

Photosynthetic reaction centres harvest the energy content of sunlight by transporting electrons across an energy transducing biological membrane. We use time-resolved serial femtosecond crystallography[1] at an X-ray free electron laser[2] to observe light-induced structural changes in the photosynthetic reaction centre of *Blastochloris viridis* on a time-scale of picoseconds. Structural perturbations are first centred upon the protein's special pair of chlorophyll molecules that are photo-oxidized by light. Electron transfer to the menaquinone acceptor on the opposite side of the membrane induces a movement of this cofactor in concert with lower amplitude protein rearrangements. These observations reveal how proteins utilize conformational dynamics to stabilize the charge separation steps of electron transfer reactions.

Our biosphere depends upon the electron transfer reactions of photosynthesis as a primary source of energy. Photosystems and photosynthetic reaction centres form a family of integral membrane protein complexes found in plants, algae, cyanobacteria and photosynthetic bacteria that convert the energy of a captured photon into a charge separated state. The photosynthetic reaction centre of the purple non-sulphur bacterium *Blastochloris viridis* (RC_{vir}) contains three transmembrane subunits called H, L and M and a periplasmic subunit C. These subunits support four bacteriochlorophyll molecules (BCh), two bacteriopheophytin molecules (BPh), a tightly bound menaquinone (Q_A), a mobile ubiquinone (Q_B), a single non-haem iron and four haem co-factors (**Fig. 1**). Electron transfer reactions originate at a special pair (SP) of strongly interacting bacteriochlorophylls which in *Bl. viridis* have an absorption maximum at 960 nm. Photo-oxidation of the SP liberates an electron which is transferred to the active branch BPh_L within a few picoseconds, is transferred to the tightly bound menaquinone (Q_A) in less than a nanosecond, and is transferred to the mobile ubiquinone (Q_B) in microseconds. SP^+ is reduced by subunit C and a second photo-oxidation event transfers a

second electron to Q_B^-, which is protonated from the cytoplasm and released into the membrane as ubiquinol (H_2Q). Other proteins participate in a cyclic flow that returns electrons to subunit C and the net effect is that two protons are transported across an energy-transducing membrane for every photon absorbed.

Electrons may tunnel between cofactors when they are separated by approximately 10 Å or less.[3] The primary electron transfer step from SP to BPh_L occurs in 2.8 ± 0.2 ps[4] over a distance of 10 Å by means of a two-step hopping mechanism *via* the monomeric BCh_L[5] and is more rapid than conventional Marcus theory. By contrast, the 9 Å electron transfer step from BPh_L to Q_A has a single exponential decay time of 230 ± 30 ps[6] which is consistent with conventional Marcus theory. Coherent nuclear motions[7] and protein structural changes[8] have been suggested to influence the initial charge-transfer reactions of photosynthesis yet the specific nature of these putative protein motions is unknown. Flash-freeze crystallographic trapping studies,[9] time-resolved Laue diffraction[10] and time-resolved serial femtosecond crystallography[11-14] (TR-SFX) have revealed structural changes in bacterial photosynthetic reaction centres[9,10] and cyanobacterial photosystem II[11-14] that occur on the late microsecond to millisecond time-scale, yet no time-resolved crystallographic studies on the time-scale of the primary charge separation reactions of photosynthesis have been reported.

Here we apply time-resolved serial femtosecond crystallography[1] at an X-ray free electron laser (XFEL) to probe the ultrafast structural response of RC_{vir} to light. We photo-excited the special pair with 150 fs pulses centred at 960 nm (Extended Data Fig. 1). X-ray pulses 40 fs in duration were generated at the LCLS[2] and were used to record diffraction patterns from tens of thousands of microcrystals for the time points Δt = 1 ps, 5 ps (two repeats), 20 ps, 300 ps (two repeats) and 8 μs after photoexcitation (Extended Data Table 1). The time point Δt = 1 ps

92 populates the photo-excited charge transfer state of the SP in which charge rearrangements
93 have occurred within the bacteriochlorophyll dimer but are prior to the primary electron
94 transfer step; Δt = 5 and 20 ps are after the initial charge-transfer step and SP is oxidized and
95 BPh_L is reduced; Δt = 300 ps is longer than the time constant for electron transfer to Q_A and
96 menaquinone is reduced; and Δt = 8 μs corresponds to a meta-stable charge separated state.
97
98 Extended Data Fig. 2 presents overviews of the $|F_{obs}|^{light}$-$|F_{obs}|^{dark}$ isomorphous difference
99 Fourier electron density maps ("light" corresponds to data collected from photo-activated
100 microcrystals whereas "dark" corresponds to data collected from microcrystals that were not
101 photo-activated) for all time points. Difference electron density features are visible above 4.0
102 σ (σ is the root mean square electron density of the map) near SP for all time points and
103 strong features associated with Q_A are visible for $\Delta t \geq$ 300 ps (Extended Data Table 2). In
104 contradistinction with ultrafast TR-SFX studies of bacteriorhodopsin,[15] photoactive yellow
105 protein,[16] rsEGFP[17] and bacterial phytochromes[18] in which ultrafast structural changes are
106 driven by the movements of atoms due to a photo-isomerization event, TR-SFX
107 measurements of RC_{vir} reveal a knock-on effect on protein structure due to the light-induced
108 redistribution of charge. Electric-field induced conformational changes have been observed
109 when fields of the order 10^8 V/m are applied across a protein-crystal[19] and this is the same
110 order of magnitude as electric field perturbations due to the movement of an electron within
111 RC_{vir}.
112
113 Recurring changes of electron density are visible as positive difference electron density in the
114 region of overlap between the two bacteriochlorophylls SP_L and SP_M of the special pair, and
115 complementary negative difference electron density features are visible primarily associated
116 with SP_M (Fig. 2, Extended Data Fig. 3, Extended Data Table 2, Supplementary Video 1).

Singular value decomposition (SVD) of all seven difference Fourier electron density maps (Fig. 2e) reveals that the strongest positive and several of the strongest negative difference electron density features of the principal SVD component are associated with the SP (Extended Data Table 2). Quantification of electron density changes[20] within the $RC_{vir.}$ co-factors (Fig. 2f) and statistical tests against control difference Fourier electron density maps (Methods) provides a very high-level of confidence (p-value ≤ 0.001, Extended data Table 3) that these recurring difference electron density features do not arise by chance. Thus photoexcitation causes the bacteriochlorophylls of SP to move closer together and the bending (an out of plane distortion) of SP_M could explain these observations. An out of plane distortion was used to model difference electron density features observed as carbon monoxide was photo-dissociated from the haem of myoglobin[21] (Extended Data Fig. 4). Nonplanar distortions of chlorin and bacteriochlorin rings are observed in photosystem II and $RC_{sph.}$ due to interactions with the surrounding protein[22] and nonplanar porphyrins are also more easily oxidized than planar porphyrins.[23,24] This suggests that the distortion of SP in advance of the primary charge separation event (Fig. 2a) could enhance the yield of the primary charge-transfer reaction, which has been optimized by evolution to achieve almost perfect quantum efficiency.[25]

When the C-subunit is fully reduced, an electron is transferred from $haem_3$ to SP^+ in less than a microsecond.[26] The above reasoning implies that SP^+ may be more easily reduced should SP_M return to a planar geometry before this electron transfer occurs. This hypothesis is consistent with our experimental observations since the amplitude of the positive difference electron density feature between the SP bacteriochlorophylls increases from Δt = 1 ps to 20 ps, decreases for Δt =300 ps and is insignificant for Δt = 8 μs (Fig. 2, Extended Data Fig. 3, Extended Data Table 2). Moreover, neither TR-SFX studies of the S2→S3 transition of

142 cyanobacteria PSII[13] (Δt = 150 μs and 400 μs) nor TR-Laue diffraction studies of RC_{vir}[10] (Δt =
143 3 ms) report a positive difference electron density feature in the region of overlap between the
144 special pair of (bacterio)chlorophylls, implying that this feature has decayed.
145
146 Charge rearrangements cause SP^+ to move up to 0.3 Å towards the M-subunit by Δt = 300 ps
147 and the side-chains of both $His173_L$ and $His200_M$ adjust to preserve their ligating interactions
148 with the magnesium ions of SP^+, as do $His168_L$ and $Tyr195_M$ adjust conformation in order to
149 maintain their H-bond interactions to SP_L and SP_M respectively. These structural perturbations
150 are revealed by paired negative and positive difference electron density features on the side-
151 chain of $His173_L$ in the principal SVD components calculated from both the early (1ps, 2 ×
152 5ps, 20 ps) and late (2 × 300 ps, 8 μs) sub-sets of TR-SFX data, whereas positive difference
153 electron density features associated with the side-chains of $His200_M$ and $Tyr195_M$ become
154 noticeably stronger for the later sub-set of data (Extended Data Fig. 3i,j; Extended Data Table
155 2; Supplementary Video 1). These observations suggest that SP_L moves towards subunit M
156 slightly in advance of SP_M, which may be due to dielectric asymmetry within photosynthetic
157 reaction centres.[27,28] Dielectric asymmetry is believed to underpin the phenomenon that
158 electron transfer occurs only along the A-branch[27] in purple bacteria RCs and PSII (Fig. 1).
159
160 An electron moves from SP to BPh_L in 2.8 ± 0.2 ps[4] and from BPh_L to Q_A in 230 ± 30 ps.[6]
161 The tightly bound menaquinone is therefore neutral for Δt = 1 ps, 5 ps and 20 ps; three-
162 quarters of the photo-activated population are reduced to semiquinone by Δt = 300 ps; and
163 essentially all photo-activated molecules have Q_A reduced at Δt = 8 μs. Our difference
164 Fourier electron density maps confirm these expectations since the few difference electron
165 density features visible within the Q_A binding pocket for $\Delta t \leq 20$ ps are isolated whereas more
166 continuous paired positive and negative difference electron density features are visible for Δt

≥ 300 ps (Fig. 3, Extended Data Fig. 5). These recurring features of the later sub-set of TR-SFX data (2 × 300 ps, 8 µs) produce strong difference electron density features in the principal SVD component that are associated with Q_A and its H-bond interaction with $His217_M$ (Extended Data Table 2, Fig. 3d, Supplementary Video 2) and statistical tests establish that these recurring changes cannot be ascribed to noise (p-value ≤ 0.0125, Extended Data Table 3). Structural refinement models these observations as due to a twist and translation of the semiquinone that brings the negatively charged head-group approximately 0.2 Å closer to the positive charge of the non-haem Fe^{2+} (Fig. 3f) and thereby stabilizes the reduced form of this cofactor. This interpretation receives support from QM/MM calculations that predict that the Q_A to $His217_M$ H-bond is shortened by 0.17 Å when Q_A is reduced (Extended Data Fig. 6f) and suggest that semiquinone binding is stabilized by approximately 36 $kJ.mol^{-1}$ due to structural changes (Extended Data Fig. 6g,h, Methods), which is a sizeable fraction of the energy (125 $kJ.mol^{-1}$) of a 960 nm photon. Similar conclusions were drawn from an earlier analysis using a Density Functional Theory (DFT) formalism.[29] Light-induced electron density changes were visible for Q_A in TR-SFX studies of the S2→S3 transition of cyanobacteria PSII[13] for the time points 150 µs and 400 µs, light-induced movements of the mobile quinone Q_B were also observed in PSII[11-14] for delays of hundreds of milliseconds, and larger light-induced motions of Q_B were reported in freeze-trapping studies of the *Rhodobacter sphaeroides* photosynthetic reaction centre.[9]

For Δt = 300 ps, paired negative and positive difference electron density features are associated with the cytoplasmic portions of TM helices D_M and E_M (Fig. 3e) and indicate that RC_{vir} adjusts its structure in response to the movement of the semiquinone within the Q_A binding pocket (Fig. 3f). A more quantitative analysis (Methods, Extended Data Fig. 7, Supplementary Video 3) suggests that low-amplitude protein motions begin to arise already

192 by Δt = 1 ps (Fig. 4a) as observed in TR-SFX studies of bR[15,20] and Mb:CO[21]; the amplitude
193 of these motions increase with time and by Δt = 5 ps larger displacements are observed near
194 the SP^+ and BPh_L^- cofactors (Fig. 4b); and for Δt = 300 ps protein conformational changes
195 extend throughout the A-branch of the electron transfer pathway from SP^+ to Q_A^- (Fig. 4c).
196 When the same representation is used to depict protein conformational changes predicted
197 from QM/MM calculations (Supplementary Video 4) almost no structural changes are
198 expected for the photo-excited charge transfer state (Fig. 4d); protein movements arise near
199 the charged cofactors in the SP^+:BPh_L^- charge-separated state (Fig. 4e); and structural changes
200 extend throughout the A-branch in the SP^+:Q_A^- charge-separated state (Fig. 4f). These
201 findings demonstrate that RC_{vir} is not a passive scaffold but rather low-amplitude protein
202 motions engage in a choreographed dance with electron movements taking the lead and
203 protein conformational changes following. Conversely, as the protein's structure adjusts to
204 stabilize these charge rearrangements the energetic barriers hindering the reverse electron
205 transfer reaction increase, thereby extending the lifetime of the change separated species and
206 enhancing the overall efficiency of photosynthesis.
207
208 In Marcus theory the total potential energy of an electron donor and its surroundings must be
209 equal to that of the electron acceptor and its surroundings if an electron is to tunnel from
210 donor to acceptor.[3] Fluctuations in the organizational energy around protein cofactors are
211 therefore essential to facilitate electron transfer reactions. Efforts aimed at understanding how
212 protein conformational dynamics control the rates of electron transfer between cofactors[8,30]
213 have been hampered by a lack of experimental tools that characterize protein structural
214 changes on the relevant time-scales. Our observations provide an experimental framework for
215 extending the standard description of electron transfer reactions in photosynthesis[3] to
216 explicitly incorporate protein structural changes. Electron transfer reactions are ubiquitous in

nature and therefore a more nuanced understanding of the interplay between protein structural dynamics and the movement of electrons has far-reaching biochemical significance.

Extended Data is available for this manuscript.

Supplementary Information is available for this manuscript.

Acknowledgements Use of the Linac Coherent Light Source (LCLS), SLAC National Accelerator Laboratory, is supported by the U.S. Department of Energy, Office of Science, Office of Basic Energy Sciences under Contract No. DE-AC02-76SF00515. Parts of the sample delivery system used at LCLS for this research was funded by the NIH grant P41GM103393, formerly P41RR001209. Complementary studies were performed at BL3 of SACLA with the approval of the Japan Synchrotron Radiation Research Institute (JASRI, proposal number 2018B8068). RN acknowledges funding from the European Commission Marie Curie Training Networks (X-Probe, NanoMem), the European Union's Horizon 2020 research and innovation programme (grant agreement No. 789030) and the Swedish Research Council (grant No. 2015-00560 and 349-2011-6485), the Swedish Foundation for Strategic Research (grant SRL10-0036), and the Knut and Alice Wallenberg Foundation (grant KAW 2012.0284, KAW 2012.0275 and KAW 2014.0275). GB acknowledges funding from the Swedish Research Council (grant 2017-06734) and the Swedish Foundation for Strategic Research (grant ID17-0060). GG and HLL acknowledge funding from the Academy of Finland (grants 290677 and 304455), the BioExcel CoE project funded by the European Union contracts H2020-INFRAEDI-02-2018-823830 and H2020-EINFRA-2015-1-675728, and the CSC-IT centre in Espoo for access to computing resources. R.N. wishes to thank Professors Neal Woodbury for discussions.

Author Information

These authors contributed equally: Robert Dods, Petra Båth.

Contributions

R.N. conceived the experiment, which was designed with input from G.B., R.D., J.D., S.B., M.L., S.C., D.M., M.S.H., G.J.W., J.D., D.P.D. and A.B. Samples were prepared by R.D., P.Bå., D.A. and R.B. Crystallization was supervised by G.B.. Time-resolved serial femtosecond crystallography experiments were performed at the LCLS by R.D., P.Bå., D.A., R.B. K.R.B., G.N., M.L., D.M., J.R., R.H., P.Be., E.M., L.J., R.A., S.C., E.C., C.E.C., P.D., G.H., M.S.H., C.L., S.L. C.S., A.S., G.J.W., C.W., J.D., D.P.D., A.B., G.B. and R.N. The CXI instrument was set up and run by M.L., M.S.H., G.J.W. and S.B.. The photoexcitation laser of 960 nm was operated and aligned by D.M., J.R., S.C. and J.D.. Sample delivery was performed by K.R.B., G.N., R.H., P.Be., P.D. and D.P.D. Data were analysed by R.D., P.Bå., A.R., O.Y., A.B., G.B. and R.N. Structural refinement was performed by R.D. and P.Bå. Resampling, full occupancy structural refinement and analysis were performed by V.A.G, G.K. and A.V. Integration within a sphere and statistical tests were performed by C.W., R.N. and P.Bå.. SVD analysis was performed by A.V. Quantum Mechanics/Molecular Mechanics analysis were performed by D.M., H.L.L and G.G.. Time-resolved IR spectroscopy measurements were performed by J.K, M.M and S.W. The manuscript was prepared by R.N., P.Bå., R.D. and G.B. with additional input from all authors.

Corresponding Author

Correspondence to Richard Neutze (richard.neutze@gu.se).

Code Availability

Software used for SVD analysis is available at https://github.com/Neutze-lab/SVD. Code written in MATLAB to analyse difference electron density amplitudes is available at

https://github.com/Neutze-lab/maptool. Software associated with the resampling of X-ray diffraction data is available at https://github.com/Katona-lab/CFEL_tools.

Data Availability

Atomic coordinates and structure factors have been deposited in the Protein Data Bank, www.pdb.org. PDB ID codes are the following: 5O4C the dark-conformation (a); 5NJ4 the dark conformation (b); 6ZHW the time-point Δt = 1 ps; 6ZI4 the time-point Δt = 5 ps (a); 6ZID the time-point Δt = 5 ps (b); 6ZI6 the time-point Δt = 20 ps; 6ZI5 the time-point Δt = 300 ps (a); 6ZI9 the time-point Δt = 300 ps (b); 6ZIA the time-point Δt =8 µs. Difference Fourier electron density maps and stream files containing X-ray diffraction intensities are deposited at the CXI database (http://www.cxidb.org/) with identification number ID 161.

Competing Interests

The authors declare no competing interests.

REFERENCES

1 Tenboer, J. *et al.* Time-resolved serial crystallography captures high-resolution intermediates of photoactive yellow protein. *Science* **346**, 1242-1246 (2014).

2 Emma, P. *et al.* First lasing and operation of an angstrom-wavelength free-electron laser. *Nat. Photon.* **4**, 641-647 (2010).

3 Marcus, R. A. & Sutin, N. Electron transfers in chemistry and biology. *Biochim. Biophys. Acta* **811**, 265-322 (1985).

4 Breton, J., Martin, J. L., Migus, A., Antonetti, A. & Orszag, A. Femtosecond spectroscopy of excitation energy transfer and initial charge separation in the reaction center of the photosynthetic bacterium Rhodopseudomonas viridis. *Proc. Natl. Acad. Sci. USA* **83**, 5121-5125 (1986).

5 Chan, C. K., DiMagno, T. J., Chen, L. X., Norris, J. R. & Fleming, G. R. Mechanism of the initial charge separation in bacterial photosynthetic reaction centers. *Proc. Natl. Acad. Sci. USA* **88**, 11202-11206 (1991).

6 Holten, D., Windsor, M. W., Parson, W. W. & Thornber, J. P. Primary photochemical processes in isolated reaction centers of Rhodopseudomonas viridis. *Biochim. Biophys. Acta* **501**, 112-126 (1978).

7 Vos, M. H., Rappaport, F., Lambry, J.-C., Breton, J. & Martin, J.-L. Visualization of coherent nuclear motion in a membrane protein by femtosecond spectroscopy. *Nature* **363**, 320-325 (1993).

8 Wang, H. *et al.* Protein dynamics control the kinetics of initial electron transfer in photosynthesis. *Science* **316**, 747-750 (2007).

9 Stowell, M. H. *et al.* Light-induced structural changes in photosynthetic reaction center: implications for mechanism of electron-proton transfer. *Science* **276**, 812-816 (1997).

10 Wöhri, A. B. *et al.* Light-induced structural changes in a photosynthetic reaction center caught by Laue diffraction. *Science* **328**, 630-633 (2010).

11 Young, I. D. *et al.* Structure of photosystem II and substrate binding at room temperature. *Nature* **540**, 453-457 (2016).

12 Suga, M. *et al.* Light-induced structural changes and the site of O=O bond formation in PSII caught by XFEL. *Nature* **543**, 131-135 (2017).

13 Kern, J. *et al.* Structures of the intermediates of Kok's photosynthetic water oxidation clock. *Nature* **563**, 421-425 (2018).

14 Suga, M. *et al.* An oxyl/oxo mechanism for oxygen-oxygen coupling in PSII revealed by an x-ray free-electron laser. *Science* **366**, 334-338 (2019).

15 Nogly, P. *et al.* Retinal isomerization in bacteriorhodopsin captured by a femtosecond x-ray laser. *Science* **361**, eaat0094 (2018).

16 Pande, K. *et al.* Femtosecond structural dynamics drives the trans/cis isomerization in photoactive yellow protein. *Science* **352**, 725-729 (2016).

17 Coquelle, N. *et al.* Chromophore twisting in the excited state of a photoswitchable fluorescent protein captured by time-resolved serial femtosecond crystallography. *Nature Chem* **10**, 31-37 (2018).

18 Claesson, E. *et al.* The primary structural photoresponse of phytochrome proteins captured by a femtosecond X-ray laser. *Elife* **9**, e53514 (2020).

19 Hekstra, D. R. *et al.* Electric-field-stimulated protein mechanics. *Nature* **540**, 400-405 (2016).

20 Wickstrand, C. *et al.* A tool for visualizing protein motions in time-resolved crystallography. *Struct Dyn* **7**, 024701 (2020).

21 Barends, T. R. *et al.* Direct observation of ultrafast collective motions in CO myoglobin upon ligand dissociation. *Science* **350**, 445-450 (2015).

22 Saito, K. *et al.* Deformation of chlorin rings in the Photosystem II crystal structure. *Biochemistry* **51**, 4290-4299 (2012).

23 Shelnutt, J. A. *et al.* Nonplanar porphyrins and their significance in proteins. *Chem. Soc. Rev.* **27** 31-42 (1998).

24 Barkigia, K. M., Chantranupong, L., SmithJ, K. M. & Fajer, J. Structural and theoretical models of photosynthetic chromophores. Implications for redox, light-absorption properties and vectorial electron flow. *J. Am. Chem. Soc.* **110**, 7566-7567 (1988).

25 Wraight, C. A. & Clayton, R. K. The absolute quantum efficiency of bacteriochlorophyll photooxidation in reaction centres of Rhodopseudomonas spheroides. *Biochim Biophys Acta* **333**, 246-260 (1974).

26 Dohse, B. *et al.* Electron transfer from the tetraheme cytochrome to the special pair in the Rhodopseudomonas viridis reaction center: effect of mutations of tyrosine L162. *Biochemistry* **34**, 11335-11343 (1995).

27 Steffen, M. A., Lao, K. & Boxer, S. G. Dielectric asymmetry in the photosynthetic reaction center. *Science* **264**, 810-816 (1994).

28 Najdanova, M., Grasing, D., Alia, A. & Matysik, J. Analysis of the Electronic Structure of the Special Pair of a Bacterial Photosynthetic Reaction Center by (13) C Photochemically Induced Dynamic Nuclear Polarization Magic-Angle Spinning NMR Using a Double-Quantum Axis. *Photochem Photobiol* **94**, 69-80 (2018).

29 Hasegawa, J.-Y. *et al.* Energetics of the Electron Transfer from Bacteriopheophytin to Ubiquinone in the Photosynthetic Reaction Center of Rhodopseudomonas Viridis: Theoretical Study. *J. Phys. Chem. B* **107**, 838-847 (2003).

30 LeBard, D. N., Martin, D. R., Lin, S., Woodbury, N. W. & Matyushov, D. V. Protein dynamics to optimize and control bacterial photosynthesis. *Chem. Sci.* **4**, 4127-4136 (2013).

FIGURE LEGENDS

Figure 1: Electron transfer steps of the photosynthetic reaction centre of *Bl. viridis.* Cartoon representation of the H, L, M and C subunits. Cofactors are shown in black including the special pair of bacteriochlorophylls (SP), two monomeric bacteriochlorophylls (BCh), two bacteriopheophytins (BPh), a tightly bound menaquinone (Q_A), a mobile ubiquinone (Q_B), a non-haem iron (Fe^{2+}) and four haems. The approximate boundaries of the membrane are suggested in blue. The electron transfer pathway: SP → BPh_L → Q_A is referred to as the A-branch. Approximate timescales for the first two electron transfer events, from SP to BPh_L and from BPh_L to Q_A, are depicted.

Figure 2: Light-induced electron density changes in RC_{vir} at the site of photo-oxidation. **a,** Experimental $F_{obs}^{light} - F_{obs}^{dark}$ difference Fourier electron density map for Δt = 1 ps. **b,** Difference Fourier electron density map for Δt = 5 ps (data set a). **c,** Difference Fourier electron density map for Δt = 20 ps. **d,** Difference Fourier electron density map for Δt = 300 ps (data set a). **e,** Principal component from SVD analysis of all seven experimental difference Fourier electron density maps. All maps are contoured at ± 3.2 σ (blue, positive difference electron density; gold, negative difference electron density; σ is the root mean square electron density of the map). **f,** Relative amplitudes of difference electron density features integrated within a 4.5 Å sphere[20] centred upon the RC_{vir} co-factors (Extended Data Fig. 3j). The colour bars represent: cyan, Δt = 1 ps; blue, Δt = 5 ps a and b (in that order); purple, Δt = 20 ps; red, Δt = 300 ps b and a (in that order); mustard, Δt = 8 μs.

Figure 3: Light-induced electron density changes in RC_{vir} within the menaquinone binding pocket. a, Experimental $F_{obs}^{light} - F_{obs}^{dark}$ difference Fourier electron density map for Δt = 5 ps (data set a). **b,** Difference Fourier electron density map for Δt = 300 ps (data set a). **c,** Principal component from SVD analysis of the first four experimental difference Fourier electron density maps (Δt = 1ps, 5 ps (a), 5 ps (b), 20 ps). **d,** Principal component from SVD analysis of the final three experimental difference Fourier electron density maps (Δt = 300 ps (a), 300 ps (b), 8 μs). All maps are contoured at ± 3.0 σ (blue, positive difference electron density; gold, negative difference electron density). **e,** Difference Fourier electron density map for Δt = 300 ps (data set a) showing the protein immediately surrounding Q_A and contoured at ± 3.5 σ. **f,** Superposition of the refined structures for the dark structure (yellow, Q_A in black) and Δt = 300 ps (purple structure).

Figure 4: Structural response of RC_{vir} to electron transfer events. a, Recurring movements of Cα atoms for Δt = 1 ps quantified by full occupancy structural refinement against 100 randomly resampled TR-SFX data sets. **b,** Recurring movements of Cα atoms for Δt = 5 ps (a) using the same representation. **c,** Recurring movements of Cα atoms for Δt = 300 ps (a) using the same representation. Recurring movements are represented as error weighted mean ratios relative to 100 control structural refinements (Methods) coloured from grey (< 80 % of the maximum error weighted mean ratio) to red (≥ 95 % of the maximum error weighted mean ratio). An identical representation is given for all time points in Extended Data Fig. 7. **d,** Movements of Cα atoms estimated from QM/MM energy minimization calculations associated with the SP photo-excited and all other cofactors in resting state: $SP^*:BPh_L^0:Q_A^0$ (Methods). **e,** Movements of Cα atoms estimated from QM/MM energy minimization calculations associated with the SP photo-oxidized and BPh_L reduced: $SP^{+1}:BPh_L^{-1}:Q_A^0$. **f,**

Movements of Cα atoms estimated from QM/MM energy minimization calculations associated with SP photo-oxidized and Q_A reduced: SP^{+1}:BPh_L^{0}:Q_A^{-1}. Movements are coloured from grey (no movements) to red (maximum Cα motions). Transmembrane helices are drawn as rods.

METHODS

Protein production and purification

The expression and purification of photosynthetic reaction centre from *Bl. viridis* cells was adapted from Wöhri et al.[31]. Cells were disrupted by three rounds of sonication followed by centrifugation in a JA20 rotor at 15000 rpm for 20 minutes to recover the membrane suspensions. Membranes were then purified by ultracentrifugation at 45000 rpm for 45 min in a Ti45 rotor. Membranes were homogenized in 20 mM Tris-HCl, pH 8.5 and diluted to OD_{1012} = 10. Membranes were then solubilized in 4 % lauryldimehtylamine-N-oxide (LDAO) for 3 hours at room temperature. Unsolubilized membranes were removed by ultracentrifugation at 45000 rpm for 75 min in a Ti70 rotor. RC_{vir} protein was purified by loading the supernatant onto a 250 ml POROS 50-µm HQ ion-exchange medium equilibrated with wash buffer (20 mM Tris-HCl, pH 8.5, 1% LDAO). The column was washed with 2 l of wash buffer with 5 % elution buffer (20 mM Tris-HCL, pH 8.5, 1 M NaCl, 1 % LDAO) and eluted with an increasing concentration of elution buffer over 20 column volumes. Fractions with an A_{280}/A_{830} < 3.5 were pooled and concentrated in 100 kDa MW cut off concentration tubes (Vivaspin) to a volume of 10 ml. This was loaded in 5ml batches onto a HiPrep 26/60 Sephacryl S-300 column (GE) equilibrated with SE buffer (20 mM Tris-HCl, pH 8.5, 100 mM NaCl, 0.1 % LDAO) and eluted into 1.8 ml fractions. Fractions with an A_{280}/A_{830} < 2.6 were pooled and concentrated, followed by a 20-fold dilution in final protein buffer (20mM NaH_2PO_4/Na_2HPO_4, pH 6.8, 0.1 % LDAO, 10 µM EDTA) and then concentrated again to 20 $mg.ml^{-1}$. Samples were flash-frozen in liquid nitrogen and stored at -80 °C.

Protein crystallization

20 µl sitting drops were set up with a 1:1 ratio of protein solution (10 $mg.ml^{-1}$) and precipitant solution (3.6 M ammonium sulphate, 6 % heptane-1,2,3-triol, 20 mM NaH_2PO_4/Na_2HPO_4, pH

6.8) set up against a 1 ml reservoir of 2 M ammonium sulphate. Large crystals grew at 4 °C in 3 days. Crystals were harvested by pipette and crushed mechanically to create a seed stock by vortexing with seed beads for approximately 20 min with occasional cooling on ice[32]. For the XFEL experiment in April 2015 (run a) new 18.5 µl sitting drop vapour diffusion crystallization drops were set up in order to yield large numbers of micro-crystals. In these experiments the protein concentration was 8.5 $mg.ml^{-1}$ and a protein:precipitant concentration of 10:7.5 was used in the drops. 1 µl of undiluted crystal seed stock was spiked into the drops for a final v/v concentration of 5.4 %. Crystallization drops were then mixed by pipette and covered with a glass cover slide. Rod-like crystals grew over 5 days at 4 °C and were 10 – 20 µm in the longest dimension. Microcrystals for the experiment in June 2016 (run b) were prepared as above, but with an additional round of microseeding using crushed microcrystals to seed an additional round of microcrystal growth[32]. Micro-crystals were harvested by pipette and concentrated up to three-fold by centrifugation at 1000 *g* for 1 min followed by removal of supernatant. These crystals were somewhat thicker and, while diffracting to higher-resolution, they highlighted the compromise inherent in TR-SFX since a lower excited-state occupancy was usually observed when working with crystals of higher optical density.

Sample injection and data collection

Microcrystals were transferred from Eppendorf tubes to a sample reservoir using a syringe and passing the microcrystal slurries through a stainless steel 20 µm filter (VICI AG International) or a 20µm nylon filter (Sysmex). The reservoir was loaded into a temperature controlled rocking chamber and injected into the XFEL through a GDVN[33] using an internal diameter of 75 µm. The microjet used a microcrystal suspension flow rate of 20 $\mu l.min^{-1}$ and was focused to a 10 µm diameter using helium gas. The X-ray beam was aligned to interact

with the liquid jet as close to the tip of the GDVN as practical and before Rayleigh breakup of the microjet.

Diffraction data were collected at 293 K at the CXI beam line[34] of the LCLS XFEL during beamtime awarded in April 2015 (run a) and June 2016 (run b). Diffraction data were recorded on a Cornell-SLAC Pixel Array detector[35]. The X-ray wavelengths and equivalent pulse energies were 1.89 Å (6.56 keV) in 2015 and 1.31 Å (9.49 keV) in 2016. An X-ray pulse duration of 36 fs was used in 2015 and 45 fs in 2016. The XFEL beam was focused to a 3 μm^2 spot for both experiments. The detector was located 89 mm from the microjet in 2015 and 145 mm from the microjet in 2016. Diffraction data were collected at a repetition rate of 120 Hz from microcrystals that were not exposed to any optical laser pump (dark-state) and for five time points corresponding to Δt = 1ps, 5 ps, 20 ps, 300 ps and 8 μs after photo-excitation. The time points Δt = 5 ps and 300 ps were repeated in both 2015 and 2016 and are referred to as data sets a and b respectively.

Laser photoexcitation

An optical Ti:Sa pump laser 150 fs in duration was focused into a spot size of 190 μm FWHM (323 μm $1/e^2$) and aligned to overlap with the LCLS X-ray pulse. The LCLS timing-tool[36] provided a timing accuracy of ± 200 fs for the time point, Δt, between the arrival of the optical pump laser and the X-ray probe. A pump-laser wavelength of 960 nm was used to photo-excite RC_{vir} microcrystals, and this wavelength is at the absorption maximum of the special pair ($\varepsilon_{960} \approx 100\,000\ M^{-1}.cm^{-1}$). The pump laser energy per pulse was 11.8 μJ in April 2015 and 11.0 μJ in June 2016. For an idealized Gaussian beam, 86.5 % of this light will pass through a spot with diameter $1/e^2$ and 50 % of this light will pass through a spot with diameter FWHM. Thus the average fluence within the FWHM spot can be estimated as 25 mJ/cm^2 and

492 23 mJ/cm^2 which equates to a pump-laser power-density of 138 GW/cm^2 for the 2015
493 experiment and 129 GW/cm^2 for the 2016 experiment. This calculation defines the units used
494 throughout to specify the laser power-density. Both values are above 30 GW/cm^2 to 100
495 GW/cm^2 that has been recommended as an upper threshold to avoid nonlinear effects in
496 bacteriorhodopsin.[37,38]
497
498 Extreme non-linear absorption was observed as ultrafast sample heating in time-resolved X-
499 ray scattering studies of RC_{vir} when pumped with 800 nm light.[39] When using 800 nm to
500 photo-excite RC_{vir} it is the BCh cofactors (rather than the SP) which absorb light ($\varepsilon_{800} \approx$
501 180 000 $M^{-1}.cm^{-1}$). The pump-laser fluence used in that study[39] was 1560 GW/cm^2. Ultrafast
502 sample heating within a GDVN liquid microjet has also been measured as a function of the
503 800 nm pump-laser fluence using time-resolved X-ray scattering (Fig. 28 of reference[40]).
504 These measurements show that the energy deposited into RC_{vir} samples is proportional to the
505 pump-laser fluence (a linear response) up to 270 GW/cm^2 and that the measured heating then
506 varies quadratically (a non-linear response) above a pump-laser fluence of 355 GW/cm^2. Thus
507 either an idealized assumptions of a perfectly aligned Gaussian beam may not be realistic,
508 and/or large losses occur as the incoming laser pulse is reflected from the surface of a GVDN
509 liquid microjet, and/or a thresholds[37,38] of 30 GW/cm^2 to 100 GW/cm^2 do not apply RC_{vir}
510 when photo-excited at 800 nm. When 960 nm light is used to photo-excite the SP of RC_{vir} it is
511 likely more difficult to induce non-linear effects because the photo-excited state SP* has an
512 absorption maximum red-shifted 70 nm relative to the ground state[41] and hole-burning[42] has
513 been observed in RC_{vir} such that SP* is effectively transparent to the incoming light.
514 Moreover, the absorbance of RC_{vir} at 960 nm is only 56 % of it absorbance at 800 nm and
515 therefore non-linear effects are likely to arise at higher power densities when using 960 nm
516 rather than 800 nm to photo-excite RC_{vir}. Non-linear ultrafast heating[40] is observed in RC_{vir}

delivered using a GDVN liquid microjet and photo-excited at 800 nm only above a power-density of 355 GW/cm$^{2.}$ Therefore the 960 nm pump-laser power-densities of 138 GW/cm^2 and 129 GW/cm^2 used in this work are below where non-linear effects may reasonably be anticipated. These conclusions are supported by time-resolved IR spectroscopy measurements (Extended Data Fig. 1).

Time-resolved infrared spectroscopy

Time-resolved vibrational spectroscopy measurements were performed with a near infrared (NIR) pump and mid-infrared (IR) probe setup using a regenerative amplifier (Spitfire Ace, Spectra Physics) to deliver pulses centred at 800 nm (1.2 mJ, 5 kHz). The amplifier output is used to pump a TOPAS-TWINS (Light Conversion) capable of generating tuneable femtosecond pulses at two different wavelengths. One path was used to generate mid-infrared probe light centred at 6000 nm via difference frequency generation whereas the other path generated 960 nm pump pulses via second harmonic generation of the idler beam. The 960 nm beam was chopped to 2.5 kHz and delayed in time relative to the probe pulses using an optical delay line. Two weak replicas derived from the midIR beam were used as probe and corresponding reference. Both probe and reference were dispersed in a Horiba spectrograph (grating with 75 gr/mm) and detected and integrated on a double-row MCT array with 64 pixels each on a shot-to-shot basis using a commercial detection system (Infrared Systems). Samples of RC_{vir} were prepared in a customized cell by enclosing ca. 15 uL of solution (RC_{vir} at ca. 0.4 mM in D_2O buffer) between two 2 mm thick CaF_2 windows separated by a 25 μm spacer. Probe and reference beams were focused at the sample position and collimated using 90° off-axis parabolic mirrors. The pump beam was focused using a 30-cm lens and overlapped with the probe beam at its focus. The sample cell was placed where pump and probe beams meet and translated continuously perpendicular to the beam direction during data

acquisition. The focal spot size of the pump beam was determined using knife-edge scans and yielded perpendicular $1/e^2$ radii of 57 µm and 56 µm. Different pump fluences were adjusted using reflective neutral density filters (Edmund Optics). For each fluence, twelve repeats over five time points (1000 pump shots per time point and repeat, at delays of -50, 1, 2, 5 and 300 ps) were recorded and less than 5% of shots were rejected during data treatment. Signals were calculated by subtracting consecutive pump-on from pump-off shots followed by application of the noise reduction algorithm.[43,44] The spectral resolution is < 5 cm^{-1}. The results of these measurements are presented in Extended Data Fig. 1.

Data processing

Images containing more than 20 diffraction spots were identified as diffraction hits by Cheetah.[45] Cheetah converted the raw detector data into the HDF5 format and data were then processed using the software suite CrystFEL version 0.6.2.[46,47] Crystals were indexed using a tetragonal unit cell (a = b = 226.4 Å, c = 113.7 Å, α = β = γ = 90º). Scaling and merging were performed using Monte Carlo methods using the same software. Data from the dark state and photo-excited states were scaled together using the custom dataset splitting option in the CrystFEL partialator module. Structure factors were calculated from merged intensities by the CCP4 module TRUNCATE[48] and molecular replacement was performed using the CCP4 module Phaser[49] using the ground-state RC_{vir} structures solved with XFEL radiation (PDB codes 5O4C and 5NJ4) as a search models. Statistics for data collection and refinement are detailed in Extended Data Table 1.

Electron density difference maps

Isomorphous $|F_{obs}|^{light}$-$|F_{obs}|^{dark}$ difference Fourier electron density maps were calculated using the refined dark state structures for phases with the time-points Δt = 5 ps (data set a) and 300

ps (data set a) calculated against data and coordinates using the pdb entry 5O4C whereas the time point with the time-points Δt = 1 ps, 5 ps (data set b), 20 ps, 300 ps (data set b) and 8 µs were calculated against data and coordinates using the pdb entry 5NJ4. Thus all difference electron density map calculations used only data collected during the same experiment. Difference Fourier electron density maps represent measured changes in X-ray diffraction intensities as changes in electron density without bias towards the photo-activated state's structural model. The technique is extremely sensitive to small changes in electron density[50] and reveals more subtle features than are apparent from $2mF_{obs}$-DF_{calc} electron density maps alone (m is the figure of merit and D is estimated from coordinate errors). A Bayesian weighting calculation script[51] using CNS software[52] was also used to analyse the difference Fourier electron density maps. In this procedure structure factor amplitude differences were weighted by the product of the figure of merit of the ground state structure reflections and of a weighting term, w (Equation 14 of reference[53]), which was calculated using Bayesian statistics developed to improve signal to noise.[53] For six of seven data-sets the recurring difference electron density features were slightly strengthened by this step. The exception was the time-point Δt = 8 µs which has difference electron density feature that are weaker than for the other maps (Fig. 2f) and appears due to a lower occupancy of the charge separated state in these microcrystals. It is possible that a fraction of the photo-oxidized SP^- population is reduced from the C-subunit by Δt = 8 µs, which is longer than the time-scale of this electron transfer step.[26] However, no efforts were made to reduce the C-subunit when preparing microcrystals and a similar occupancy (30% ± 5%) is observed to persist in time-resolved spectroscopy measurements on crystals for up to millisecond delays.[10]

Singular value decomposition

SVD analysis of difference Fourier electron density maps was performed using an in-house code written in python that is based upon an approach previously described.[54] As has been discussed,[55] SVD may serve as a noise-filter to enhance the signal across a sequence of difference Fourier electron density maps. This step contains the assumption that the overall mechanism is linear and that changes in electron density are similar over the selected time-windows. When applying SVD we evaluate the expression [U,Σ,V] = SVD(A), where A is a matrix of n difference Fourier electron density maps containing m elements; U is an n × n unitary matrix; Σ is an n × m rectangular matrix containing n diagonal elements (the singular values) arranged in decreasing order and all other matrix elements are zero; and the first right singular vector (the first row of the matrix V) is referred to as the principal component. Results from SVD analysis of all seven electron density maps are presented in Fig. 2e and Extended Data Fig. 3l,m. Results from SVD analysis deriving from the first four time-points (Δt = 1 ps, 5 ps a and b, 20 ps) and the last three time-points (Δt = 300 ps a and b, 8 μs) are shown in Fig. 3c,d; Extended Data Fig. 3h,i; Extended Data Fig. 5h,i; Supplementary Videos 1 and 2. This separation of the maps is motivated by the fact that photo-activated RC_{vir} molecules have menaquinone oxidized for the first sub-set of time-points yet most menaquinone molecules of photo-activated RC_{vir} are reduced for the second sub-set of time-points.

Structural refinement of photo-excited states

Isomorphous $|F_{obs}|^{light}$-$|F_{obs}|^{dark}$ difference Fourier electron density maps were inspected in COOT. Structural refinement was performed using Phenix.[56] A model was first placed within the unit cell using rigid body refinement followed by multiple rounds of partial-occupancy refinement where the SP, BCh_L, BPh_L, Q_A, portions of TM helices E_L, D_L, E_M and D_M, as well as connecting loops, and additional residues near cofactors (L153-178, L190, L230, L236-

248, M193-221, M232, M243-253, M257-266) were allowed to adopt a second conformation with 30 % occupancy and the dark-state structure (pdb entry 5O4C) was held fixed. The occupancy of 30 % was chosen by assessing the results from partial occupancy refinement when the occupancy was allowed to vary and was imposed for all structural refinements for consistency. Results from structural refinement were compared against the difference electron densities and some manual adjustments were made using COOT.[57] Refinement statistics are displayed in Extended Data Table 1. Validation of structure geometry was performed using MOLPROBITY[58] and PROCHECK.[59] Structural changes were also validated by calculating simulated difference Fourier electron density maps from the refined structures[10,20] (Extended Data Figs. 2l and 4j).

Structural analysis of large-scale protein motions

The high multiplicity of SFX data was exploited for structural analysis by randomly selecting a sub-set of experimental observations from within each SFX data-set to create 100 separate (but not independent) serial crystallography data-sets for the two resting state data-sets and the seven photo-activated data-sets, amounting to 900 resampled data-sets in total. For each of these resampled data-sets the mean and uncertainty estimates (σ) for every unique Bragg reflection were determined. Structural refinement over a cycle of 100 rigid body and 100 isotropic restrained refinements with all atoms allowed to move and with every atom having 100 % occupancy were then performed against each of these 900 resampled data-sets using pdb entry 5NJ4 as a starting model. R_{free} values ranging from 22.1 % to 23.1% were recovered. Coordinate errors associated with each individual structural refinement are estimated[60] to be $\leq$ 0.2 Å.

The distances between the Cα atoms of the photo-activated and resting RC_{vir} structures were compared pairwise using the miller package of CCTBX.[61] A 100×100 Euclidian distance matrix was then calculated for every Cα atom and every time point according to: $\Delta r_{ij}^{\Delta t,dark} = |\mathbf{r}_i^{\Delta t} - \mathbf{r}_j^{dark}|$, where *i* and *j* vary from 1 to100 and denote resampled dataset numbers, $\Delta r_{i,j}$ depicts the distance separating the Cα coordinates of datasets *i* and *j*, and $\mathbf{r}_i^{\Delta t}$ and $\mathbf{r}_j^{dark}$ are the refined coordinates obtained from the photo-activated or dark structures, respectively. A second order Taylor series expansion was then used to estimate the mean and error associated with the ratio $\Delta r_{ij}^{\Delta t,dark}/\Delta r_{ij}^{dark,dark}$ arising from coordinate variations within each set of 100 structural refinements. This expansion leads to the expression:

$$\text{Error weighted mean ratio} = \langle \Delta r_{ij}^{state,dark} \rangle / \langle \Delta r_{ij}^{dark,dark} \rangle$$

$$- \text{var}(\Delta r_{ij}^{dark,dark}) \times \langle \Delta r_{ij}^{state,dark} \rangle / \langle \Delta r_{ij}^{dark,dark} \rangle^3 + \text{cov}(\Delta r_{ij}^{state,dark}, \Delta r_{ij}^{dark,dark}) / \langle \Delta r_{ij}^{dark,dark} \rangle^2$$

where <X> is the mean of the set X, var(X) is the variance of the set X, and cov(X,Y) is the covariance of two sets X and Y. The resulting error weighted mean ratios are represented in Fig. 4A to 4C and Extended Data Fig. 7 in which movements are coloured from grey (movements ≤ 80 % of the maximum ratio) to red (movements ≥ 95 % of the maximum ratio). Full occupancy structural refinement avoided systematic bias in this analysis arising from partial occupancy structural refinement with a single dark-conformation held fixed, but at the cost of underestimating the magnitude of light-induced conformational changes. Despite this limitation, this analysis extracted recurring structural motions that evolve with time (Fig. 4a-c and Extended Data Fig. 7, Supplementary Video 3) and in a manner that is both consistent with the known time-scales of the electron transfer reactions (Fig. 1) and theoretical predictions (Fig. 4d-f, Supplementary Video 4).

Tests of the statistical significance of recurring difference electron density features

For each of the seven experimental difference Fourier electron density maps (Δt = 1 ps, 5 ps (data set a), 5 ps (data set b), 20 ps, 300 ps (data set b), 300 ps (data set a), 8 μs) a lower-pedestal of 3.0 σ was applied such that all electron density with an amplitude < 3.0 σ was set to zero. Both positive and negative difference electron densities were then integrated within a 4.5 Å radius sphere about a chosen coordinate (Extended Data Fig. 3j) as described for the analysis of TR-SFX data recorded from bacteriorhodopsin.[20] These positive (A+) and negative (A-) integrated difference electron density amplitudes were merged to yield a single amplitude according to: $A(\mathbf{r}) = ((A+)^2+(A-)^2)^{½}$ about the centre of integration **r**. The results of this analysis are presented in Fig. 2f where six centres of integration, **r**, are chosen as: the centre of the BPh_M ring; the magnesium atom of BCh_M; the mid-point between the two magnesium atoms of the two SP bacteriochlorophylls; the magnesium atom of BCh_L; the centre of the BPh_L ring; and the centre of the ketone containing six-carbon ring of menaquinone Q_A.

For tests of statistical significance (Extended Data Table 3), this set was complemented by the addition of amplitudes extracted by integration about the iron atoms of $haem_1$, $hame_2$, $haem_3$ and $haem_4$ to create a set of ten amplitudes for each of the seven time points:

$$[A(BPh_M), A(BCh_M), A(SP), A(BCh_L), A(BPh_L), A(Q_A),A(H_1),A(H_2),A(H_3),A(H_4)]_{\Delta t}$$

arranged as a 10 × 7 element matrix. Control "noise only" $|F_{obs}|^{dark}$-$|F_{obs}|^{dark}$ isomorphous difference Fourier electron density maps were calculated by first selecting sixteen resampled data-sets from the set of 100 generated from the 2015 RC_{vir} dark data, and sixteen resampled data-sets from the set of 100 generated from the 2016 RC_{vir} dark data. Eight $|F_{obs}|^{dark}$-$|F_{obs}|^{dark}$ isomorphous difference Fourier electron density maps were then calculated by pair-wise comparisons between the sixteen resampled data-sets of the 2015 data, and another eight difference Fourier electron density maps were calculated by pairwise-comparisons of the

sixteen resampled data-sets of the 2016 data. Seven control difference Fourier electron density maps were then randomly selected from the set of sixteen "noise-only" maps, difference electron density values with an amplitude lower than 3σ were set to zero, and a set of [A(**r**,dark-dark)] were created by integrating the remaining difference electron density within a 4.5 Å radius sphere centred upon the RC_{vir} cofactors as described above. A two-sample *t*-test was then performed in MATLAB to determine if the set of seven time-dependent amplitudes [A(**r**,Δ*t*)] and the set of seven "noise-only" amplitudes [A(**r**,dark-dark)] were indistinguishable from one another (the null hypothesis). The *t*-tests were then repeated 1000 times by randomly selecting a different combination of seven control amplitudes [A(**r**,dark-dark)] from the sixteen "noise-only" difference Fourier electron density maps calculated above (of 16!/(9!×7!) = 11440 possible different combinations of the 16 control maps). The results of this analysis are summarized in Extended Data Table 3 and show that, when a threshold of $p \leq 0.001$ is applied, the difference electron density amplitudes associated with the SP cannot be ascribed to noise. When a threshold of $p \leq 0.0125$ is applied and the last three time-points (Δ*t* = 300 ps (a), 300 ps (b), 8 μs) are examined as a set, the difference electron density amplitudes associated with the SP, BCh_L and Q_A cannot be ascribed to noise. Conversely, the set of difference electron density amplitudes associated with most other co-factors, as well as all sets of difference electron density amplitudes generated from noise-only maps, are indistinguishable from noise according to the results of this two sample *t*-test (Extended Data Table 3).

QM/MM Geometry optimizations

Initial coordinates were taken from PDB databank entry 5O4C and missing residues and co-factor segments were retrieved from PDB entry 1PRC.[62] Protonation states of residues were chosen based on their reference pK_a values and structural criteria such as hydrogen bond

714 interactions. After the addition of protons to the structure, a 200 step steepest descent
715 geometry optimization was performed with Gromacs 4.5[63] to relax these coordinates. During
716 this optimization the positions of the heavy atoms were constrained to their positions in the x-
717 ray structure. As in previous work, the interactions were modelled with the Amber03 force-
718 field.[64,65] Non-bonded Coulomb and Lennard-Jones interactions were evaluated without
719 periodic boundary conditions (PBC) and using infinite cut-offs.
720
721 After relaxing hydrogens with molecular mechanics (MM) optimization, we performed
722 several Quantum Mechanics (QM)/MM geometry optimizations of all atoms in the reaction
723 centre, using the interface between the TeraChem quantum chemistry package[66,67] and
724 Gromacs 4.5.[63] These optimizations were also performed without PBC and with infinite cut-
725 offs for the Coulomb and Lennard-Jones interactions. The QM subsystems (Extended Data
726 Fig. 6a-c) were modelled with unrestricted DFT. In these DFT calculation we used the PBE0
727 functional[68] in combination with the LANL2DZ basis set.[69] Empirical corrections to
728 dispersion energies and interactions were introduced with Grimme's DFT-D3 model.[70] The
729 remainder of the protein, including crystal water molecules, was modelled with the Amber03
730 force-field,[64,65] in combination with the TIP3P water model.[71] We searched for minimum-
731 energy geometries in all relevant oxidation states of the system using the limited-memory
732 Broyden-Fletcher-Goldfard-Shannon quasi-Newton optimization algorithm.
733
734 The goal of these optimization steps was to characterize the structural relaxation of the protein
735 in response to changes in the electronic states of the cofactors along the A-branch of the
736 photo-induced electron transfer process. We therefore examined the following electronic
737 configurations:
738 i. All cofactors in their resting states: SP^0, BPh_L^0, Q_A^0

ii. Special pair photo-excited, other cofactors in resting state: SP*, BPh_L^0, Q_A^0

iii. Special pair photo-oxidized, BPh_L reduced: SP^{+1}, BPh_L^{-1}, Q_A^0

iv. Special pair photo-oxidized, Q_A reduced: SP^{+1}, BPh_L^0, Q_A^{-1}

Since including all co-factors into one large QM-region is computationally too demanding, we performed the optimizations with a different QM subsystem for each co-factor, including nearest residues, in all relevant electronic states. The structural response to the change in electronic state (Fig. 4d-f) was obtained by comparing the optimized geometries and potential energies in the various oxidation states.

To quantify the effect of photo-absorption by the special pair (SP, i to ii) we first optimized the resting state with the SP plus nearby residues in the QM region (Extended Data Fig. 6a), described at the PBE0/LANL2DZ level of theory plus D3 dispersion corrections. This structure was used as a reference for the optimized structures in the excited state (SP*, ii) and after photo-oxidation (SP^{+1}, iii). Using the same QM/MM subdivision, we optimized the system in the first singlet excited state (S_1) by switching the QM description to the Time-dependent DFT within the Tamm-Dancoff approximation,[72] and in the photo-oxidized state by switching the spin state of the electronic wave function to the lowest energy doublet state (D_0). In the QM/MM optimization of the D_0 state of the SP, we modelled the BPh_L with point charges representing the reduced state of that co-factor. Only very modest protein structural changes were associated with the optimized geometries with the SP in the S_1 and D_0 relative to the reference structure in the resting state (S_0). Likewise, we also optimized the geometry of the protein with the BPh_L and nearby residues in the QM region (Extended Data Fig. 6d) in both the lowest energy singlet (S_0, i) and doublet (D_0, reduced, iii) states. In the optimization of the D_0 state of BPh_L, the partial charges on the SP were changed to reflect its photo-

763 oxidized (D_0, SP^{+1}) state. Again the structural response is rather minor, as the geometries are
764 very similar (Extended Data Fig. 6e).
765
766 In the next step of the electron transfer process, the electron transfers from BPh_L to Q_A (iv).
767 We optimized the protein with Q_A plus its immediate environment, including the non-heme
768 Fe^{2+} site, in the QM region. The optimized structures in the resting and reduced states are
769 compared in Extended Data Fig. 6f. Reduction of Q_A from menaquinone to (deprotonated)
770 semiquinone induces significant structural changes in the Q_A binding pocket. In line with the
771 difference densities observed at 300 ps after photo-excitation, the hydrogen bond between the
772 Q_A carbonyl and $His217_M$ reduces by 0.17 Å. We suggest that the reduction of this hydrogen
773 bond helps stabilizing the negative charge on the Q_A.
774
775 To quantify the overall structural response to the electron transfers, we computed the
776 displacements of the atoms in the various states (ii-iv) with respect to the structure of resting
777 state (i) and recorded these displacements as B-factors to the pdb coordinate file of the resting
778 state. Because only one co-factor was included in the QM region of our QM/MM
779 optimizations, we summed up the displacements of both QM/MM optimizations of each redox
780 state. Fig. 4d-f represents these displacements as colours.
781
782 *Stabilization energies*
783 To estimate the energetic effects of the protein structural changes on the electron transfer
784 process, we computed the adiabatic and vertical electron affinities for Q_A in isolation and in
785 the optimized QM/MM protein models. These energies are shown schematically in Extended
786 Data Fig. 6g,h. For the neutral Q_A in vacuum, the electron affinity *without* structural
787 relaxation is 164.5 $kJ.mol^{-1}$ (vertical electron affinity, VEA). Structural relaxation in response

788 to adding the electron increases the affinity further by 24 kJ.mol^{-1}, so that the energy
789 difference between the neutral reactant minimum on the one hand and the reduced product
790 minimum is 188.5 kJ.mol^{-1} (adiabatic electron affinity, AEA) on the other hand. The
791 calculated AEA is in good agreement with results from previous computations,[29] but is an
792 overestimation with respect to the experimental value for the related 1,4-naphthoquinone (175
793 kJ.mol^{-1}).[73] Inside the protein environment, the VEA is much higher (258 kJ.mol^{-1}), part of
794 which we attribute to the electrostatic interaction between the reduced Q_A co-factor with the
795 positively charged Fe^{2+} ligand site. Structural relaxation of both the Q_A cofactor and the
796 protein environment increases the electron affinity by 60 kJ.mol^{-1} to yield an AEA of 318
797 kJ.mol^{-1}. Thus, the results of the computations suggest that the structural response of the
798 protein adds another 36 kJ.mol^{-1} to the intrinsic relaxation energy of Q_A (24 kJ.mol^{-1} in
799 vacuum) as concluded in earlier computations.[29] We note that in this analysis we focussed
800 only on the effect of the structural response on the affinity of Q_A. To estimate the *total*
801 reaction energy associated with the photo-induced electron transfer process from the SP to
802 Q_A, we also need the absolute energies of the neutral, photo-excited and oxidized states of the
803 SP as well as the neutral and reduced states of BPh_L. However, since these energies were not
804 computed with identical QM/MM setups, we do not provide an accurate estimate here.
805
806
807
808

METHODS REFERENCES

31 Wöhri, A. B. *et al.* Lipidic sponge phase crystal structure of a photosynthetic reaction center reveals lipids on the protein surface. *Biochemistry* **48**, 9831-9838 (2009).

32 Dods, R. *et al.* From Macrocrystals to Microcrystals: A Strategy for Membrane Protein Serial Crystallography. *Structure* **25**, 1461-1468 (2017).

33 DePonte, D. P. *et al.* Gas dynamic virtual nozzle for generation of microscopic droplet streams. *J. Phys. D: Appl. Phys.* **41**, 195505 (2008).

34 Liang, M. *et al.* The Coherent X-ray Imaging instrument at the Linac Coherent Light Source. *J Synchrotron Radiat* **22**, 514-519 (2015).

35 Hart, P. *et al.* The CSPAD megapixel x-ray camera at LCLS. *Proc. SPIE* **8504C**, 85040C□85011 (2012).

36 Harmand, M. *et al.* Achieving few-femtosecond time-sorting at hard X-ray free-electron lasers. *Nature Phot.* **7**, 215-218 (2013).

37 Nass Kovacs, G. *et al.* Three-dimensional view of ultrafast dynamics in photoexcited bacteriorhodopsin. *Nat Commun* **10**, 3177 (2019).

38 Miller, R. J. D., Pare-Labrosse, O., Sarracini, A. & Besaw, J. E. Three-dimensional view of ultrafast dynamics in photoexcited bacteriorhodopsin in the multiphoton regime and biological relevance. *Nat Commun* **11**, 1240 (2020).

39 Arnlund, D. *et al.* Visualizing a protein quake with time-resolved X-ray scattering at a free-electron laser. *Nat Methods* **11**, 923-926 (2014).

40 Arnlund, D. *X-ray free-electron laser based methods for structural and ultrafast dynamics studies of a photosynthetic reaction centre* PhD thesis, University of Gothenburg, (2014).

41 Fleming, G. R., Martin, J. L. & Breton, J. Rates of primary electron transfer in photosynthetic reaction centres and their mechanistic implications. *Nature* **333**, 190-192 (1988).

42 Meech, S. R., Hoff, A. J. & Wiersma, D. A. Role of charge-transfer states in bacterial photosynthesis. *Proc Natl Acad Sci U S A* **83**, 9464-9468 (1986).

43 Feng, Y., Vinogradov, I. & Ge, N. H. General noise suppression scheme with reference detection in heterodyne nonlinear spectroscopy. *Opt Express* **25**, 26262-26279 (2017).

44 Feng, Y., Vinogradov, I. & Ge, N. H. Optimized noise reduction scheme for heterodyne spectroscopy using array detectors. *Opt Express* **27**, 20323-20346 (2019).

45 Barty, A. *et al.* Cheetah: software for high-throughput reduction and analysis of serial femtosecond X-ray diffraction data. *J. Appl. Crystallogr.* **47**, 1118-1131 (2014).

46 White, T. A. *et al.* CrystFEL: a software suite for snapshot serial crystallography. *J. Appl. Crystallogr.* **45**, 335-341 (2012).

47 White, T. A. *et al.* Recent developments in CrystFEL. *J. Appl. Crystallogr.* **49**, 680-689 (2016).

48 French, S. & Wilson, K. Treatment of Negative Intensity Observations. *Acta Crystallogr A* **34**, 517-525 (1978).

49 McCoy, A. J. *et al.* Phaser crystallographic software. *J. Appl. Crystallogr.* **40**, 658-674 (2007).

50 Henderson, R. & Moffat, J. K. The Ditferenee Fourier Technique in Protein Crystallography: Errors and their Treatment. *Acta Crystallogr. B* **27**, 1414-1420 (1971).

51 Wickstrand, C., Dods, R., Royant, A. & Neutze, R. Bacteriorhodopsin: Would the real structural intermediates please stand up? *Biochim Biophys Acta* **1850**, 536-553 (2015).

52 Brunger, A. T. *et al.* Crystallography & NMR system: A new software suite for macromolecular structure determination. *Acta Crystallogr D Biol Crystallogr* **54**, 905-921 (1998).

53 Ursby, T. & Bourgeois, D. Improved Estimation of Structure-Factor Difference Amplitudesfrom Poorly Accurate Data. *Acta Crystallogr. A.* **53**, 564-575 (1997).

54 Rajagopal, S., Schmidt, M., Anderson, S., Ihee, H. & Moffat, K. Analysis of experimental time-resolved crystallographic data by singular value decomposition. *Acta Crystallogr D Biol Crystallogr* **60**, 860-871 (2004).

55 Schmidt, M., Rajagopal, S., Ren, Z. & Moffat, K. Application of singular value decomposition to the analysis of time-resolved macromolecular x-ray data. *Biophys J* **84**, 2112-2129 (2003).

56 Adams, P. D. *et al.* PHENIX: a comprehensive Python-based system for macromolecular structure solution. *Acta Crystallogr. D Biol. Crystallogr.* **66**, 213-221 (2010).

57 Emsley, P. & Cowtan, K. Coot: model-building tools for molecular graphics. *Acta Crystallogr. D Biol. Crystallogr.* **60**, 2126-2132 (2004).

58 Chen, V. B. *et al.* MolProbity: all-atom structure validation for macromolecular crystallography. *Acta Crystallogr. D Biol. Crystallogr.* **66**, 12-21 (2010).

59 Laskowski, R. A., MacArthur, M. W., Moss, D. S. & Thornton, J. M. PROCHECK: a program to check the stereochemical quality of protein structures. *J. Appl. Cryst.* **26**, 283-291 (1993).

60 Murshudov, G. N. & Dodson, E. J. Simplified error estimation a la Cruickshank in macromolecular crystallography. *CCP4 Newsletter on protein crystallography* **33**, 31-39 (1997).

882 61 Grosse-Kunstleve, R. W., Sauter, N. K., Moriarty, N. W. & Adams, P. D. The
883 Computational Crystallography Toolbox: crystallographic algorithms in a reusable
884 software framework. *J. Appl. Cryst.* **35**, 126-136 (2002).
885 62 Deisenhofer, J., Epp, O., Sinning, I. & Michel, H. Crystallographic refinement at 2.3
886 A resolution and refined model of the photosynthetic reaction centre from
887 Rhodopseudomonas viridis. *J. Mol. Biol.* **246**, 429-457 (1995).
888 63 Pronk, S. *et al.* GROMACS 4.5: a high-throughput and highly parallel open source
889 molecular simulation toolkit. *Bioinformatics* **29**, 845-854 (2013).
890 64 Duan, Y. *et al.* A point-charge force field for molecular mechanics simulations of
891 proteins based on condensed-phase quantum mechanical calculations. *J. Comput.*
892 *Chem.* **24**, 1999-2012 (2003).
893 65 Ceccarelli, M., Procacci, P. & Marchi, M. An ab initio force field for the cofactors of
894 bacterial photosynthesis. *J. Comput. Chem.* **24**, 129-142 (2003).
895 66 Ufimtsev, I. S. & Martinez, T. J. Quantum Chemistry on Graphical Processing Units.
896 3. Analytical Energy Gradients, Geometry Optimization, and First Principles
897 Molecular Dynamics. *J Chem Theory Comput* **5**, 2619-2628 (2009).
898 67 Titov, A. V., Ufimtsev, I. S., Luehr, N. & Martinez, T. J. Generating Efficient
899 Quantum Chemistry Codes for Novel Architectures. *J Chem Theory Comput* **9**, 213-
900 221 (2013).
901 68 Adamo, C. & Barone, V. Toward Reliable Density Functional Methods without
902 Adjustable Parameters: The PBE0 Model. *J. Chem. Phys.* **110**, 6158-6170. (1999).
903 69 Dunning T.H. & P.J., H. in *Methods of Electronic Structure Theory. Modern*
904 *Theoretical Chemistry,* Vol. 3 (ed Schaefer H.F.) (Springer, 1977).

70 Grimme, S., Antony, J., Ehrlich, S. & Krieg, H. A consistent and accurate ab initio parametrization of density functional dispersion correction (DFT-D) for the 94 elements H-Pu. *J Chem Phys* **132**, 154104-154101 - 154104-154119 (2010).

71 Jorgensen, W. L., Chandrasekhar, J., Madura, J. D., Impey, R. W. & Klein, M. L. Comparison of simple potential functions for simulating liquid water. *J. Chem. Phys.* **79**, 926–935 (1983).

72 Hirata, S. & Head-Gordon, M. Time-Dependent Density Functional Theory within the Tamm–Dancoff Approximation. *Chem. Phys. Lett.* **314**, 291-299 (1999).

73 Heinis, T., Chowdhury, S., Scott, S. L. & Kebarle, P. Electron Affinities of Benzo-, Naphtho-, and Anthraquinones Determined from Gas-Phase Equilibria Measurements. *J. Am. Chem. Soc.* **110**, 400-407 (1988).

74 Maiti, S. *et al.* Femtosecond coherent transient infrared spectroscopy of reaction centers from Rhodobacter sphaeroides. *Proc Natl Acad Sci U S A* **91**, 10360-10364 (1994).

75 Pawlowicz, N. P. *et al.* Identification of the first steps in charge separation in bacterial photosynthetic reaction centers of Rhodobacter sphaeroides by ultrafast mid-infrared spectroscopy: electron transfer and protein dynamics. *Biophys J* **95**, 1268-1284 (2008).

EXTENDED DATA FIGURE LEGENDS

Extended Data Figure 1: Dependence of transient infrared (IR) spectra on the pump laser fluence. a, Time-resolved IR difference spectra recorded from RC_{vir} in D_2O buffer for four time points and variable pump-laser fluence following 960 nm excitation. Spectral changes are consistent with earlier reports.[74,75] Dominant time-dependent features are highlighted and include: (1) a negative band at 1687 cm^{-1} (9-carbonyl stretch in SP_L and SP_M) and (2) a broad negative band centred at 1680 cm^{-1} (9-carbonyl stretch in BCh_L). Transient changes from Δt = 2 ps to 5 ps correlate with the time-dependent photo-oxidation of SP. Grey columns indicate decreasing bands whereas cyan columns indicate increasing bands. **b,** Time resolve IR difference spectra normalized and superimposed. These spectra remain superimposable throughout the pump-laser fluence domain probed. **c,** Dependence of the magnitude of the difference IR signal (calculated as the sum of the absolute value over all pixels) on the pump laser fluence. Below 20 GW/cm² the absolute signal increases approximately linearly whereas above 60 GW/cm² the signal flattens out as a plateau is reached. This plateau is consistent with the complete bleaching of the special pair absorption at 960 nm in the photoexcited state and correlates with the phenomenon of hole-burning in RC_{vir}.[42]

Extended Data Figure 2: Overview of the experimental $F_{obs}^{light} - F_{obs}^{dark}$ difference Fourier electron density maps calculated between the photo-excited and resting state data. a, Overview of the structure of RC_{vir} when viewed from the plane of the membrane. TM helices E_L and D_M are highlighted in red and gold respectively. **b-h**, Difference Fourier electron density maps for the time-points: **b,** Δt = 1 ps; **c,** Δt = 5 ps (a); **d,** Δt = 5 ps (b); **e,** Δt = 20 ps; **f,** Δt = 300 ps (b); **g,** Δt = 300 ps (a); **h,** Δt = 8 µs. All maps are contoured at ± 4.0 σ

952 (σ is the root mean square electron density of the map). Positive difference electron density is
953 shown in blue and negative difference electron density is shown in gold.
954
955 **Extended Data Figure 3: Light-induced electron density changes in RC_{vir} at the site of**
956 **photo-oxidation**. Experimental $F_{obs}^{light} - F_{obs}^{dark}$ isomorphous difference Fourier electron
957 density maps for the time-points: **a,** Δt = 1 ps. **b,** Δt = 5 ps (data set a); **c,** Δt = 5 ps (data set
958 b). **d,** Δt = 20 ps; **e,** Δt = 300 ps (data set b); **f,** Δt = 300 ps (data set a); **g,** Δt = 8 μs. **h-i**,
959 Principal component from SVD analysis of difference Fourier electron density maps for: **h,**
960 the first four time-points, Δt = 1ps, 5 ps (data set a), 5 ps (data set b) and 20 ps; **i,** the final
961 three time-points, Δt = 300 ps (data set a), 300 ps (data set b) and 8 μs. All maps are
962 contoured at ± 3.2 σ (blue, positive difference electron density; gold, negative difference
963 electron density). Peak heights listed in Table 2 are marked with coloured circles in panels h
964 and i. **j,** Representation of a sphere of radius 4.5 Å used to integrate difference electron
965 density above a pedestal of 3.0 σ as described in reference[20]. Positive difference density
966 amplitudes (A+) and negative difference density amplitudes (A-) were merged according to
967 $((A+)^2+(A-)^2)^{½}$ and are displayed in Fig. 2f. These integrated difference electron density
968 values are also used in the statistical analyses presented in Extended Data Table 2. **k,**
969 Simulated difference Fourier electron density maps near the SP calculated from the refined
970 structure for Δt = 20 ps versus the refined resting state structure. Data are cut at 2.8 Å
971 resolution for comparison with experimental data. The simulated map is contoured at ± 12.0
972 σ. **l**, Relative magnitude of the singular values resulting from SVD analysis of the difference
973 Fourier electron density maps for all seven time-points. **m**, First (blue) and second (red)
974 columns of the unitary matrix U resulting from SVD analysis of all seven time-points
975 weighted according to their corresponding singular values. The first right singular vector (the
976 principal SVD component) makes a significant and positive contribution to all time-points. In

977 contrast the difference electron density maps for Δt = 5ps (a) and 300 ps (a) contain strong
978 negative contributions from the second right singular vector, which suggests that differences
979 between the two experimental runs cause systematic differences in the difference Fourier
980 electron density maps that are separated by SVD analysis.
981
982 **Extended Data Figure 4: Electron density changes near the active site of myoglobin.** The
983 $F_{obs}^{light} - F_{obs}^{dark}$ difference Fourier electron density map for Δt = 10 ps was calculated from
984 data (pdb entries 5CNE minus 5CMV) recorded during TR-SFX studies of the photo-
985 dissociation of carbon monoxide from the active site of myoglobin.[21] **a,** Data from 15 Å to 1.8
986 Å were used to calculate the difference Fourier electron density map. **b,** Data from 15 Å to 3.0
987 Å were used to calculate the difference Fourier electron density map. Positive and negative
988 difference electron density features associated with the heme group indicate slight motions of
989 the protoporphyrin-IX. Blue represents positive difference density (contoured at 3.0 σ) and
990 gold represents negative density (contoured at -3.0 σ). At 1.8 Å the maximum amplitude of
991 the highlighted difference density features are: a+, 14.5 σ; a-, 14.0 σ; b+, 4.6 σ; b- 4.0 σ; c+,
992 4.1 σ, c- 4.0 σ; d+, 3.8 σ. When the map is recalculated after data is cut to 3.0 Å resolution the
993 corresponding values are: a+, 11.9 σ; a-, 12.4 σ; b+, 4.2 σ; b- 4.1 σ; c+, 3.7 σ, c- 2.9 σ; d+, 3.2
994 σ.
995
996 **Extended Data Figure 5: Light-induced electron density changes in RC_{vir} within the**
997 **menaquinone binding pocket**. Experimental $F_{obs}^{light} - F_{obs}^{dark}$ difference Fourier electron
998 density maps for the time-points: **a,** Δt = 1 ps. **b,** Δt = 5 ps (data set a); **c,** Δt = 5 ps (data set
999 b). **d,** Δt = 20 ps; **e,** Δt = 300 ps (data set b); **f,** Δt = 300 ps (data set a); **g,** Δt = 8 µs. All seven
1000 maps are contoured at ± 3.0 σ (blue, positive difference electron density; gold, negative
1001 difference electron density). **h-i**, Principal component from SVD analysis of difference

Fourier electron density maps for: **h,** the first four time-points, Δt = 1ps, 5 ps (data set a), 5 ps (data set b) and 20 ps; **i,** the final three time-points, Δt = 300 ps (data set a), 300 ps (data set b) and 8 μs. SVD difference Fourier maps are contoured at ± 3.2 σ. Peak heights listed in Table 2 are indicated in panel i. **j,** Simulated difference Fourier electron density maps near Q_A calculated from the refined structure for Δ*t* = 300 ps (data set a) versus the refined resting state structure. Data are cut at 2.8 Å resolution for comparison with experimental data. The simulated map is contoured at ± 12.0 σ.

Extended Data Figure 6: Results of QM/MM energy minimization calculations. a-c, QM subsystems used in the QM/MM optimizations of the co-factors. Atoms included in the QM region are shown in ball-and-stick representation, while the other atoms of the protein are shown as cartoons. Atoms belonging to the co-factor that are not included in the QM region are shown as sticks. Water molecules that are not part of the QM region are not shown. **a,** Atoms included in the QM region associated with the SP. **b,** Atoms included in the QM region associated with the BPh_L. **c,** Atoms included in the QM region associated with the Q_A. **d,** Structures of the energy minimized resting conformation (black: SP and BPh_L neutral) and that after the first electron transfer step (blue: SP^{+1} and BPh_L^{-1}) shown near the special pair. **e,** Structures of the energy minimized resting conformation (black: SP and BPh_L neutral) and that after the first electron transfer step (blue: SP^{+1} and BPh_L^{-1}) shown near BPh_L. **f,** Structures of the energy minimized resting conformation (black: SP and Q_A neutral) and that after the second electron transfer step (blue: SP^+ and Q_A^-) shown near Q_A. The H-bond between O_1 of the reduced semiquinone and $N_{\delta 1}$ of $His217_M$ is predicted to be shortened by 0.17 Å when menaquinone is reduced. **g-h,** Schematic depiction of the potential energy surfaces for menaquinone in vacuum (**g**) and within the protein (**h**) in the resting (neutral) electronic state (black) and the reduced electronic state (red). Vertical electron affinities (VEA), adiabatic

electron affinities (AEA) and relaxation energies E_r were computed at the PBE0-D3/LANL2DZ level of DFT for isolated Q_A and at the PBE0-D3/LANL2DZ/Amber03 QM/MM level for Q_A within the protein.

Extended Data Figure 7: Recurring movements of Cα atoms quantified by structural refinement. Recurring movements of Cα atoms quantified by full occupancy structural refinement against 100 randomly resampled TR-SFX data sets. Recurring movements are represented as error weighted mean ratios relative to 100 control structural refinements (Methods). Error weighted means ratios are coloured from grey (< 80 % of the maximum ratio) to red (≥ 95 % of the maximum ratio). **a,** Recurring movements of Cα atoms associated with refinements against data for Δt = 1 ps. **b,** Recurring movements of Cα atoms for Δt = 5 ps (data set a). **c,** Recurring movements of Cα atoms for Δt = 5 ps (data set b). **d,** Recurring movements of Cα atoms for Δt = 20 ps. **e,** Recurring movements of Cα atoms for Δt = 300 ps (data set b). **f,** Recurring movements of Cα atoms for Δt = 300 ps (data set a). **g,** Recurring movements of Cα atoms for Δt = 8 μs. Transmembrane helices are drawn as rods.

FOOTNOTES TO EXTENDED DATA TABLES

Extended Data Table 1: Crystallographic data and refinement statistics

Footnotes to Extended Data Table 1

†$R_{split} = 1/\sqrt{2\ \frac{\sum hkl\ |\boldsymbol{I}even-\boldsymbol{I}odd|}{1/2\sum hkl\ |\boldsymbol{I}even+\boldsymbol{I}odd|}}$

‡Values in parenthesis is those of the highest resolution shell.

£Ratio of the number of indexed images to the total number of images.

Extended Data Table 2: Difference Fourier electron density peak amplitudes

Footnotes to Extended Data Table 2

*Positive and negative difference electron density peaks are marked on Extended data Figs. 3h, 3i and 5i. Difference electron density values were read out manually in COOT. Amplitudes < 2.4 σ are not shown.

Extended Data Table 3: Two sample t-tests of integrated electron density amplitudes

Footnotes to Extended Data Table 3

*Mean σ/sphere represents the root-mean-square of the difference electron density above and below a threshold of ± 3.0 σ within a sphere of radius 4.5 Å centred on the Mg^{2+} atoms of the BChs; the Fe atoms of the haems; and ring centres of the menaquinone and BPhe cofactors. All values are scaled relative to a mean value for SP = 1.

†The number of elements in each sampled set of the two-sample t-test.

‡Difference electron density associated with $haem_3$ gave the lowest mean σ/sphere (0.14) and an exceptionally low standard deviation (± 0.06). Randomly generated control data gave the corresponding values of 0.09 ± 0.22. The coincidence of a set with a low standard deviation being compared against a control set with an exceptionally high standard deviation frequently yielded low *p*-values. Nevertheless, the experimental difference features associated with $haem_3$ are weak and are therefore not physically meaningful.

£Thirty two control data sets were generated by randomly selecting a sub-set of the dark observations to generate a new data set. Sixteen control difference Fourier electron density maps were then calculated between two of the control data-sets to generate maps representing the noise inherent within the SFX experiment. Mean σ/sphere calculations and all other steps proceeded as with the light versus dark experimental difference Fourier electron density maps.

€The reference set consisted of a set of seven maps ($N_B = 7$) randomly selected from sixteen control maps. Random selection of the control set and the t-test was repeated 1000

times, from a possible set of 16!/(9!×7!) = 11440 different combinations of the 16 control maps. Percentage values give the fraction of occasions when p ≤ threshold for the resulting two sample t-test.

[$]The hypothesis that the two sets of the t-test are indistinguishable is either true (0) or false (1) at the specified confidence level.

[§] Features identified as distinguishable from noise with a degree of confidence defined by the given *p*-value.

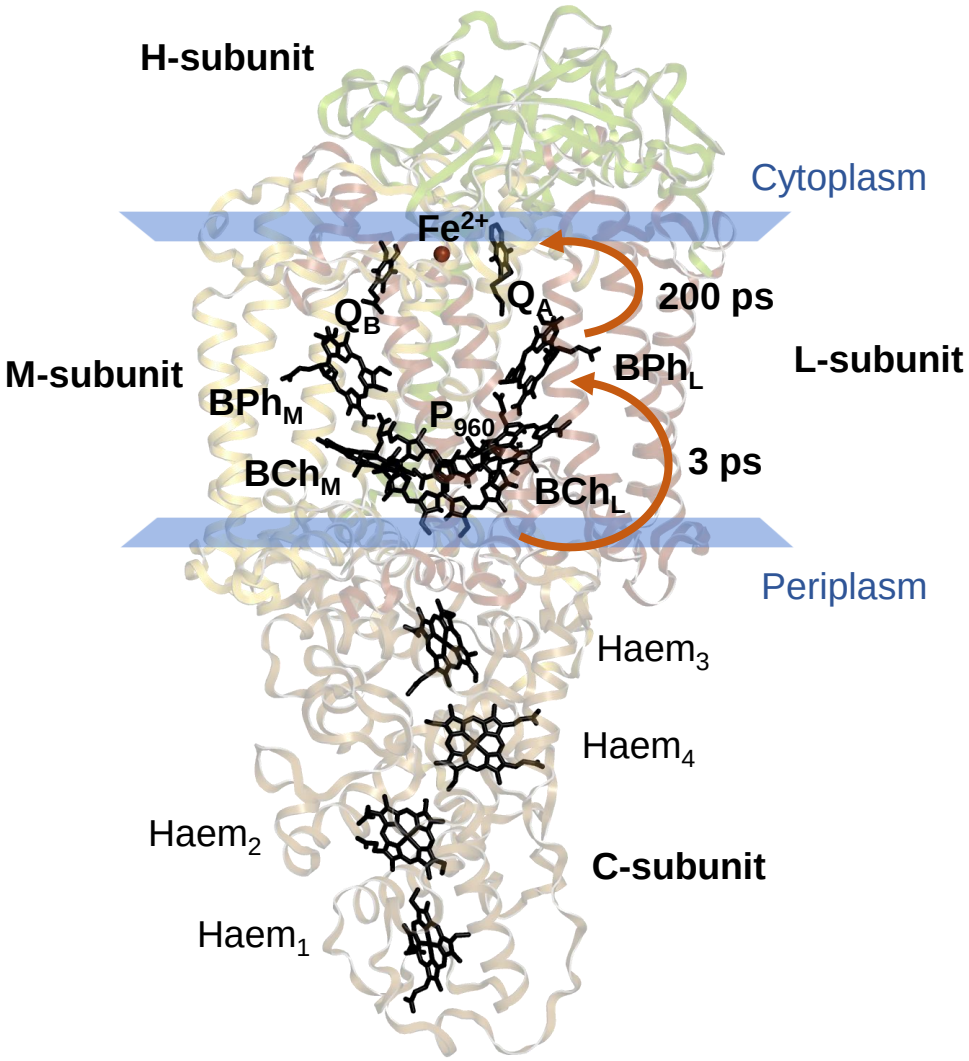

Figure 1: Dods et al.

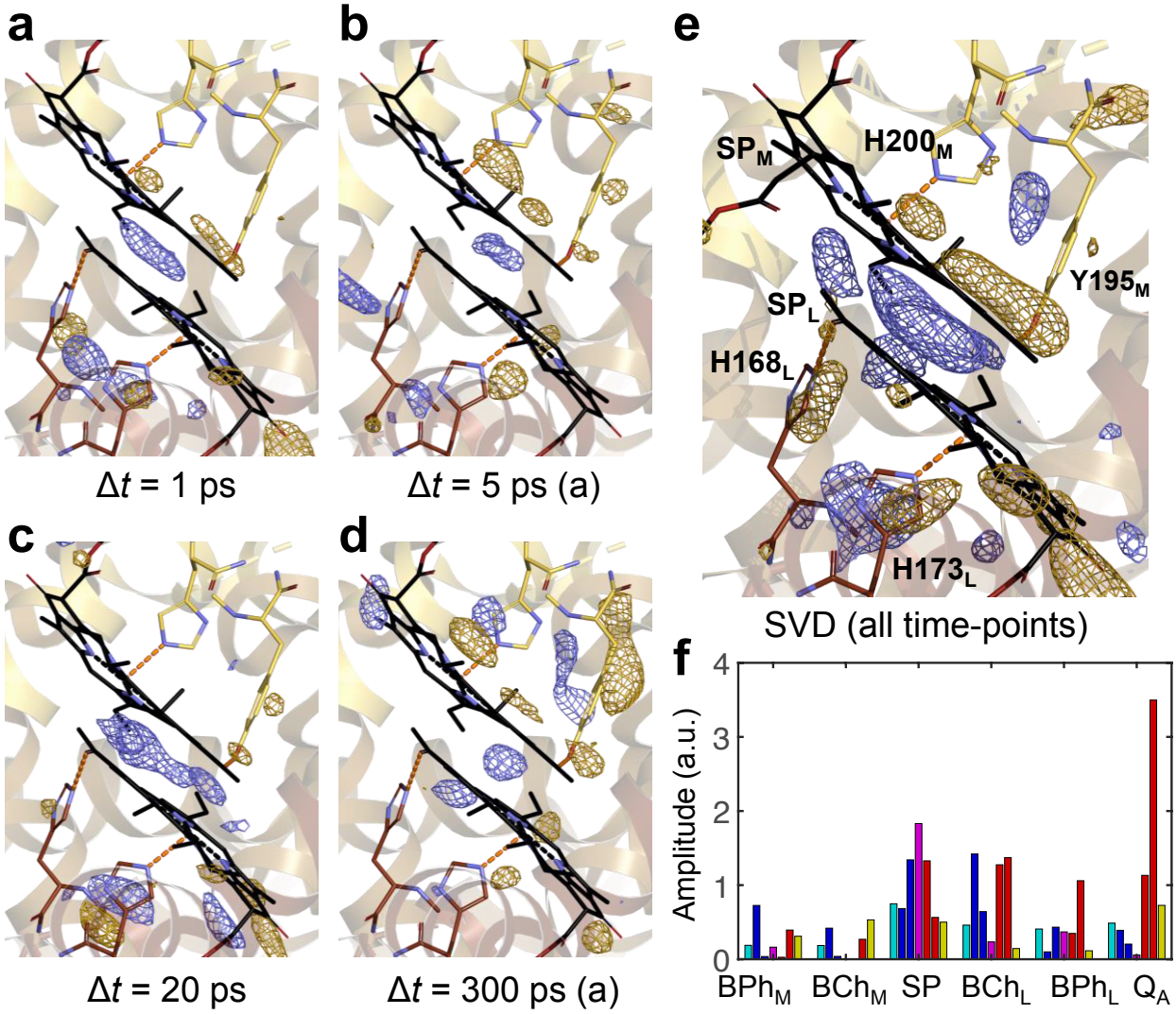

Figure 2: Dods et al.

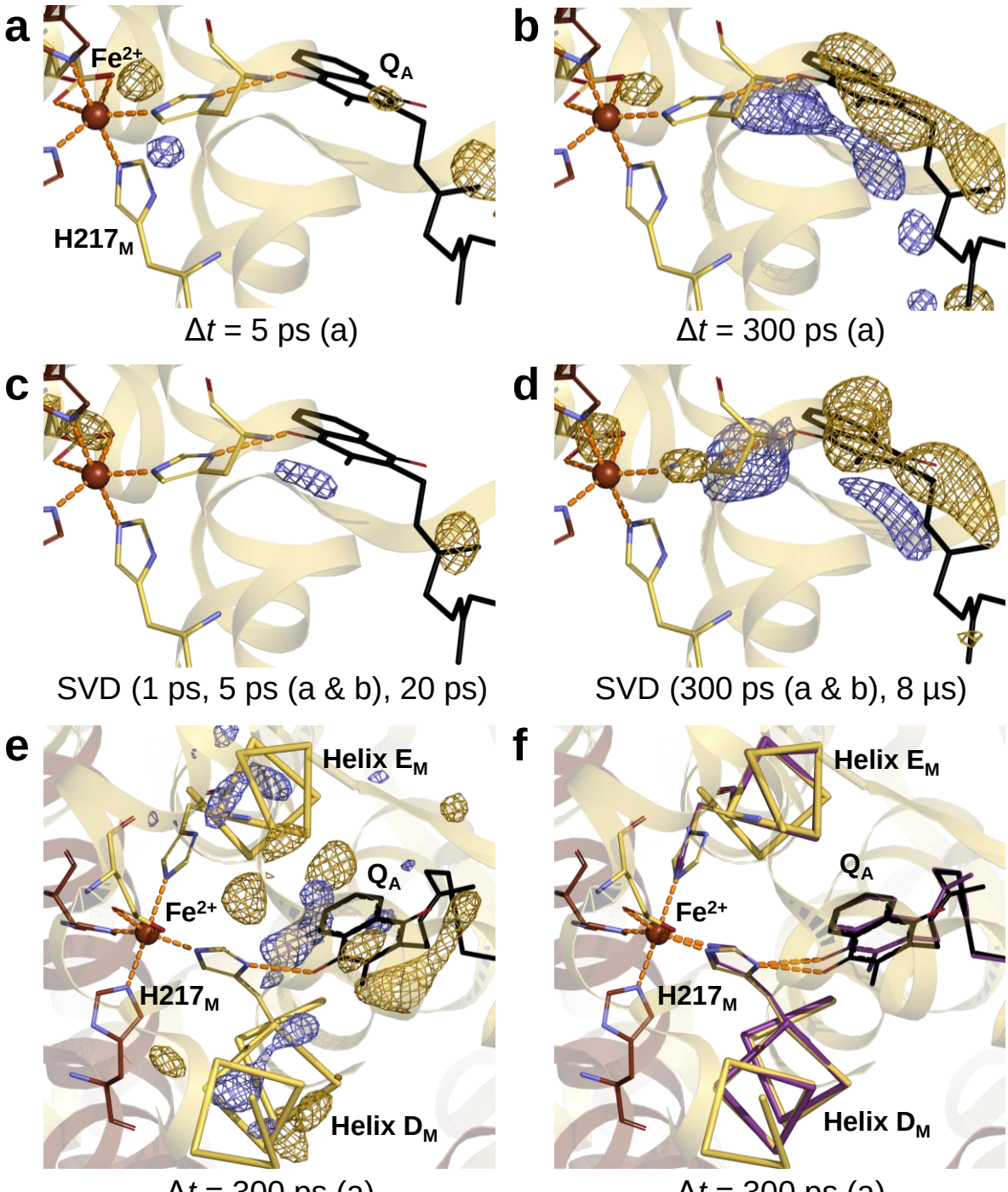

Figure 3: Dods et al.

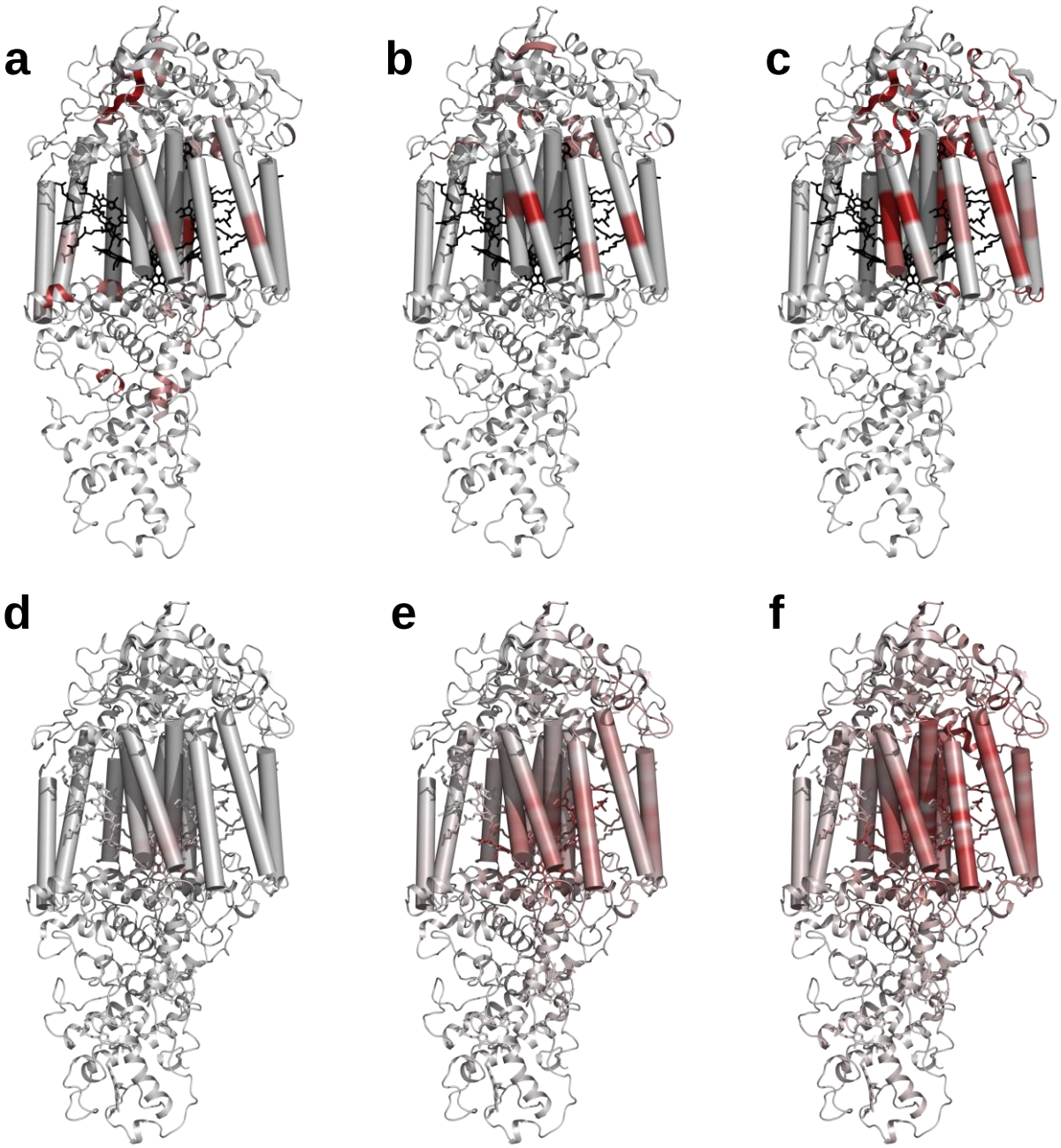

Figure 4: Dods et al.